Earth and Planetary Science Letters 467 (2017) 89–98

Contents lists available at ScienceDirect

Earth and Planetary Science Letters

www.elsevier.com/locate/epsl

Lithosphere erosion and continental breakup: Interaction of extension, plume upwelling and melting

Alessio Lavecchia [a,b,*], Cedric Thieulot [b], Fred Beekman [b], Sierd Cloetingh [b], Stuart Clark [a]

[a] Simula Research Laboratory, Fornebu, Norway
[b] Department of Earth Sciences, Utrecht University, Utrecht, The Netherlands

ARTICLE INFO

Article history:
Received 10 January 2017
Received in revised form 23 March 2017
Accepted 24 March 2017
Available online 5 April 2017
Editor: J. Brodholt

Keywords:
continental extension
lithosphere erosion
continental rift
mantle plume
melting
asymmetric margins

ABSTRACT

We present the results of thermo-mechanical modelling of extension and breakup of a heterogeneous continental lithosphere, subjected to plume impingement in presence of intraplate stress field. We incorporate partial melting of the extending lithosphere, underlying upper mantle and plume, caused by pressure–temperature variations during the thermo-mechanical evolution of the conjugate passive margin system. Effects of melting included in the model account for thermal effects, causing viscosity reduction due to host rock heating, and mechanical effects, due to cohesion loss. Our study provides better understanding on how presence of melts can influence the evolution of rifting. Here we focus particularly on the role of melting for the temporal and spatial evolution of passive margin geometry and rift migration. Depending on the lithospheric structure, melt presence may have a significant impact on the characteristics of areas affected by lithospheric extension. Pre-existing lithosphere heterogeneities determine the location of initial breakup, but in presence of plumes the subsequent evolution is more difficult to predict. For small distances between plume and area of initial rifting, the development of symmetric passive margins is favored, whereas increasing the distance promotes asymmetry. For a plume-rifting distance large enough to prevent interaction, the effect of plumes on the overlying lithosphere is negligible and the rift persists at the location of the initial lithospheric weakness. When the melt effect is included, the development of asymmetric passive continental margins is fostered. In this case, melt-induced lithospheric weakening may be strong enough to cause rift jumps toward the plume location.

1. Introduction

Processes leading to extension and rifting of lithosphere result from the interaction between mantle flow and plate movements, and involve different factors acting simultaneously. Among them, heat transfer, lithosphere structure, far field stresses, mantle flow and possibly magmatism can play a major role in determining the evolution pattern of rifting areas (e.g. Koptev et al., 2015, and ref. therein). These factors are capable of interacting, with significant feedback effects as a result, which are often difficult to predict. Plate boundary forces and lithosphere distribution are strongly influenced by mantle drag (Burov et al., 2007). At the same time the lithosphere exerts a profound effect on mantle flow (e.g. Guillou-Frottier et al., 2012).

Slab pull and roll-back, ridge push and frictional resistance provide a major contribution in the force balance controlling the plate dynamics (Bott and Kusznir, 1979). However, the role of other factors in influencing rifting style and evolution is still a matter of debate. Among these, the presence of mantle plumes is recognized as capable of playing an important role during lithosphere extension (e.g. Buck, 2004). Lithosphere impingement by the plumes may produce regional uplift driving extensional stresses (e.g. Burov et al., 2007; Burov and Gerya, 2014). Furthermore, plumes are often associated with small-scale convective instability and thermos-mechanical lithosphere erosion (e.g. Fischer and Gerya, 2016). However, previous studies (e.g. Schubert et al., 2001) show that ridge push forces, associated with mantle upwelling and resulting topographic doming, are small, or progressively decrease in comparison with plate-related far field forces. Therefore, far field forces may constitute a significant component for the development of large scale rifting and may generate the driving stress field for rift evolution (Koptev et al., 2015).

In this context, stresses causing lithosphere thinning and breakup can be divided in an “active” component, generated by mantle plumes impacting against the base of the lithosphere (e.g. Bott and Kusznir, 1979), and a “passive” component, related to

* Corresponding author.
E-mail address: alessio@simula.no (A. Lavecchia).

http://dx.doi.org/10.1016/j.epsl.2017.03.028
0012-821X/

plate movement and interaction (e.g. Cloetingh and Wortel, 1986). However, many rifting areas cannot be strictly classified in terms of either one of these two end-member components (e.g. Huismans et al., 2001; Ziegler and Cloetingh, 2004, and ref. therein).

Continental breakup leads to the creation of passive margins, with a structure reflecting their rifting development (e.g. Huismans et al., 2001; Huismans and Beaumont, 2011; Franke, 2012; Brune et al., 2014, 2016; Svartman Dias et al., 2015). Particular features of passive margins to be addressed are the magnitude of lithospheric stretching, asymmetry and magmatism. These characteristics may be strongly influenced by the presence of mantle plumes, not only due to the thermo-mechanical erosion that plumes exert at the base of the lithosphere (e.g. Burov et al., 2007; Burov and Gerya, 2014), but also due to the connection between plume presence and magmatic activity in magma-rich margins. The latter is characterized by the presence of significant volumes of melts intruding into and extruding onto the lithosphere (e.g. Menzies et al., 2002). As suggested by analytical/numerical studies (e.g. Buck, 2004) and field evidence (e.g. Wright et al., 2012), an intimate relationship may exist between rifting episodes and melts emplacement, resulting in an extension accommodated by magma filling. However, melts may result from both plumes and "plume head" upwelling (Hill, 1991), and from passive upwelling related to stretching and thinning of the lithosphere (White and McKenzie, 1989). So far, the thermo-mechanical effects of magma intrusion and underplating at lithosphere-scale remain largely unquantified, although its important role in the evolution of the crust and lithosphere has long been recognized (Ziegler and Cloetingh, 2004, and ref. therein).

Another aspect that characterizes lithospheric extension is that rift areas may be non-stationary. Many examples are documented of rift migration and jumps, especially when rifting interacts with plumes (e.g. Wilson and Hey, 1995; Einardsson, 2008). The relationships between ridge position and melt presence has been investigated in previous studies (Mittelstaedt et al., 2008), but plumes may also impinge the more heterogeneous continental lithosphere, with subsequent interaction between lithospheric structure and plume material (e.g. Bosworth et al., 2005).

In this paper we present a thermo-mechanical model for continental lithospheric extension, characterized by the presence of intra-lithospheric heterogeneities and impinged by a mantle plume. The novel aspect of this model is the incorporation of partial melting for mantle materials, as a response to pressure–temperature variations. Melts migrate upwards in response to a density difference and are emplaced at the base of the lithosphere, when their density is higher than the host rocks. Where intruded, their presence leads to a decrease of the temperature-dependent viscosity and a loss of cohesion of host rocks. Our model allows assessment of the importance of melts during the evolution of rifting areas, including the most favorable conditions that maximize their effects.

2. Model setting

2.1. Model geometry and governing equations

We constructed a 2D visco-plastic model, simulating a continental lithosphere subjected to a constant, extensional velocity, where an upper mantle layer and a plume at the base of the model are incorporated (Fig. 1). The model has a width of 1000 km and a thickness of 400 km (that is, the base of the model is constrained to the top of the mantle transition zone). It comprises 1) a two-layered crust with thickness 40 km, corresponding to an average continental crust thickness (e.g. Philpotts and Ague, 2009), where both the upper and lower crust have the same thickness (20 km), 2) a mantle lithosphere with a thickness of 80 km (e.g. Philpotts and Ague, 2009), and 3) a 280 km thick upper mantle. The shape of the plume at the onset of the simulation is a semicircle with a radius of 100 km (cf. e.g. Burov et al., 2007; Burov and Gerya, 2014). In addition, a lithosphere weakness is introduced at the boundary between lower crust and lithospheric mantle, as a square of dimension 10 km constituted by a different material from the lithosphere (see Table 1). The adopted configuration is designed for case studies where lithospheric heterogeneities occur due to the pre-rift tectonic history of the study areas. This is the case of Afar Rift, where Pan-African orogenic structures are reactivated during the Tertiary tectonic evolution, regardless of the relative plume position northward (e.g. Chorowicz et al., 1998; Bosworth et al., 2005, and ref. therein).

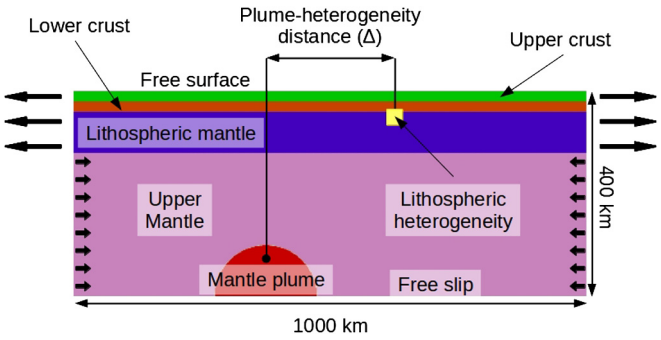

Fig. 1. Schematic representation of the model. The black arrows indicate the direction of applied velocity and relative mass outflow/inflow (see Table 1 for the adopted value).

The centers of the plume and the lithospheric weakness are equidistant from the central vertical axis of the model, and their mutual distance Δ is a parameter investigated in different simulation sets (Fig. 1). The lithosphere is subjected to an extensional velocity of 5 mm/yr at both sides of the model, compatible with slow spreading ridges and breakup areas (e.g. Wolfenden et al., 2004; McClusky et al., 2010). This velocity is appropriate for the initial configuration of the model, since larger velocities would determine a well-defined rifting area before the arrival of the plume at the base of the lithosphere, solely controlled by the position of the lithospheric weakness. Such a configuration would limit the study of the interaction between plume and lithosphere structure. The applied velocity on the lithosphere results in a mass outflow at both lateral boundaries of the model, and is counterbalanced by a mass inflow that keeps the simulation volume constant (Fig. 1). The bottom boundary condition is free slip, while a free surface is incorporated at the top boundary. Other parameters are listed in Table 1.

The code used for our simulation sets is ELEFANT, a nonlinear fluid Arbitrary Lagrangian–Eulerian (ALE) code, specifically designed for the solution of visco-plastic flow at lithospheric scale. The code is based on the algorithm already implemented in FANTOM (e.g. Thieulot, 2011), and assumes that, at a regional scale of observation and at geologic time scale, earth materials may be treated within the realm of continuum mechanics and inertial forces may be neglected (i.e. the flow Reynold number is $\approx$0) (e.g. Gerya, 2010). It derives that the momentum equation may be expressed as:

$$\nabla \cdot \boldsymbol{\sigma} + \rho \boldsymbol{g} = \boldsymbol{0} \tag{1}$$

where $\boldsymbol{\sigma}$ is the stress tensor, ρ is the density and $\boldsymbol{g}$ is the gravity acceleration vector. Materials are assumed incompressible, implying zero divergence of the velocity $\boldsymbol{v}$ tensor:

$$\nabla \cdot \boldsymbol{v} = 0 \tag{2}$$

The stress tensor $\boldsymbol{\sigma}$ can be separated into a spherical part $p\boldsymbol{1}$ and a deviatoric part $\boldsymbol{s}$, as follows:

Table 1
Thermo-mechanical parameters adopted in the model.

Surface temperature	20 °C
Temperature at the base of the lithosphere	1200 °C–1300 °C
Temperature at the base of the model	1400 °C–1475 °C
Excess temperature plume	200 °C
Extensional velocity	5 mm yr^{-1}
Thermal conductivity	2.5 W m^{-1} K^{-1} (crust), 3.5 W m^{-1} K^{-1} (lithosphere and mantle)
Heat capacity melt	771 J kg^{-1} K^{-1}
Radiogenic heat production at surface	2 μW m^{-3}
Characteristic depth for radiogenic heat production	14 km
Depleted mantle density	3325 kg m^{-3}
Melt density	2950 kg m^{-3}
Cohesion	20 MPa
Angle of friction	15°

	Material parameters					
	Upper crust (wet quartz)	Lower crust (wet plagioclase)	Lithospheric mantle (dry olivine)	Upper mantle (dry olivine)	Plume (dry olivine)	Lithospheric weakness (dry olivine)
Pre-exponential parameter [MPa^{-n} s^{-1}]	$1.1 \cdot 10^{-28}$ [a]	$3.98 \cdot 10^{-16}$ [b]	$2.41 \cdot 10^{-16}$ [c]	$2.41 \cdot 10^{-16}$ [c]	$2.41 \cdot 10^{-16}$ [c]	$1.1 \cdot 10^{-28}$ [a]
Exponent	4 [a]	3 [b]	3.5 [c]	3.5 [c]	3.5 [c]	4 [a]
Activation energy [kJ mol^{-1}]	223 [a]	356 [b]	540 [c]	540 [c]	540 [c]	223 [a]
Activation volume [kJ Pa^{-1}]	0	0	0	$5 \cdot 10^{-9}$ (df) [c] $2 \cdot 10^{-8}$ (dl) [c]	$5 \cdot 10^{-9}$ (df) [c] $2 \cdot 10^{-8}$ (dl) [c]	0 [a]
Grain size [m]	10^{-3}	10^{-3}	10^{-3}	10^{-3}	10^{-3}	10^{-3}
Grain size exponent	0	0	2.5	2.5	2.5	0
Density ($\rho 0$) [kg m^{-3}]	2800	2900	3325	3300	3275	3325

[a] Gleason and Tullis, 1995; [b] Rybacki and Dresen, 2000; [c] Karato and Wu, 1993; activation volumes: df = diffusion creep; dl = dislocation creep.

$$\boldsymbol{\sigma} = -p\mathbf{1} + \boldsymbol{s} \tag{3}$$

where $\mathbf{1}$ is the unit tensor and p is the hydrostatic pressure (Thieulot, 2011).

The deviatoric part $\boldsymbol{s}$ of the stress tensor $\boldsymbol{\sigma}$ is related to the strain rate tensor $\dot{\varepsilon}$, according to the relationship:

$$\boldsymbol{s} = 2\mu\dot{\boldsymbol{\varepsilon}} \tag{4}$$

where μ is the dynamic viscosity and $\dot{\boldsymbol{\varepsilon}}$ is given by:

$$\dot{\boldsymbol{\varepsilon}} = \left(\nabla \boldsymbol{v} + (\nabla \boldsymbol{v})^T\right)/2 \tag{5}$$

Based on the equations (1)–(5), it is possible to obtain the following form of the Stokes equation:

$$\nabla \cdot \left(\mu\left(\nabla \boldsymbol{v} + \nabla \boldsymbol{v}^T\right)\right) - \nabla p + \rho \boldsymbol{g} = \mathbf{0} \tag{6}$$

Equation (6) expresses that changes in buoyancy and constitutive relationship in any point of the domain affect the entire domain.

Earth material properties depend on temperature. Consequently, the temperature field has to be taken into account during the computation. The conservation of energy equation is then:

$$\rho C_p \left(\frac{\partial T}{\partial t} + \boldsymbol{v} \cdot \nabla T\right) = \nabla \cdot (k \nabla T) + H_r + H_m \tag{7}$$

where C_p is the heat capacity (J kg^{-1} K^{-1}), T is the temperature (K), k is the thermal conductivity (W m^{-1} K^{-1}), H_r is the internal heat production due to radioactive decay (J m^{-3} s^{-1}) and H_m is the heat released by melts at emplacement levels. This term will be further described in the following sections.

2.2. Rheology

The code used for our simulations adopts a visco-plastic rheology for earth materials. A more detailed description of the adopted methodology is given in Thieulot (2011, Appendix B). The plastic behavior is modeled here for rocks at a relatively low temperature condition, and it is approximated by a viscous deformation following the Drucker–Prager criterion (see e.g. Kachanov, 2004; Thieulot, 2011). Obtained viscosity values are given by the following equation:

$$\mu_{PL} = \frac{P \sin \Phi + C \cos \Phi}{2\dot{\varepsilon}_{II}} \tag{8}$$

where μ_{PL} is the plastic viscosity, C in the cohesion term, P is the pressure and Φ is the friction angle and $\dot{\varepsilon}_{II}$ is the second invariant of the strain rate tensor (cf. Burov and Gerya, 2014). Viscosity values are locally adapted to limit the stress generated during the deformation. For further details, see Thieulot (2011, Appendix B).

Strain weakening has been incorporated by following a linear relationship between accumulated strain in the deforming rocks and values of cohesion C and angle of friction Φ: when the accumulated strain is less that a given threshold value ε_1, C and Φ are maintained as constant. For accumulated strain values between ε_1 and ε_2, both C and Φ decrease to values Csw and Φsw, and these values are kept for accumulated strain values higher than ε_2. For further details, see Thieulot (2011, and references therein).

At higher temperature, rocks experience nonlinear viscous deformation, expressed by a temperature and stress/strain rate dependent viscosity. The relationships between stress and strain rate are described by the following equations for dislocation and diffusion creep (e.g. Gerya, 2010):

$$\dot{\varepsilon}_{II,DISL} = A\sigma_{II}^n \exp\left(-\frac{E + pV}{RT}\right) \tag{9}$$

$$\dot{\varepsilon}_{II,DIFF} = A\mathrm{h}^m \exp\left(-\frac{E + pV}{RT}\right) \tag{10}$$

where $\dot{\varepsilon}_{II,DISL}$ and $\dot{\varepsilon}_{II,DIFF}$ are the strain rate second invariant for diffusion and dislocation creep, A, n, m, V and E are material parameters, h is the grain size, σ_{II} is the stress second invariant, R in the gas constant and T is the temperature. The adopted values of parameters are given in Table 1.

Basing on the equations (9), (10), the viscosity values are calculated for dislocation and diffusion creep:

$$\mu_{DISL} = A^{-\frac{1}{n}} \dot{\varepsilon}^{\frac{1-n}{n}} \exp\left(\frac{E + pV}{nRT}\right) \tag{11}$$

$$\mu_{DIFF} = A^{-1} h^{-m} \exp\left(\frac{E + pV}{RT}\right) \tag{12}$$

and averaged to calculate the effective viscosity μ_{EFF}:

$$\mu_{EFF} = \left(\frac{1}{\mu_{PL}} + \frac{1}{\mu_{DISL}} + \frac{1}{\mu_{DIFF}}\right)^{-1} \tag{13}$$

2.3. Density model

The model implements a temperature-dependent density, according to the equation:

$$\rho_S(T) = \rho_0\big(1 - \alpha(T - T_0)\big) \tag{14}$$

where $\rho_S(T)$ is the rock density at the modeled temperature T, ρ_0 and T_0 are the reference density and temperature and α is the thermal expansion coefficient. The materials subjected to partial melting also experience an increase in density, depending on the melt fraction that is extracted during the whole simulation history. The density increase follows the equation:

$$\rho(T) = \rho_S(T)(1 - \varphi_{P,T}) + \rho_{DM}\varphi_{P,T}\big(1 - \alpha(T - T_0)\big) \tag{15}$$

where $\rho(T)$ is density of the rock subjected to partial melting, ρ_{DM} is the density value of depleted mantle (see Table 1) and $\varphi_{P,T}$ is the melt fraction obtained at different values of temperature and pressure. The details of the procedure for calculating $\varphi_{P,T}$ are provided in Section 2.4.

A density correction is also applied for materials subjected to melt intrusion, which experience a density decrease according to the equation:

$$\rho(T) = \rho_S(T)(1 - \varphi_{P,T}) + \rho_M\varphi_{P,T} \tag{16}$$

where ρ_M corresponds to the density of intruded melts (see Table 1).

2.4. Partial melting

Our model includes partial melting for mantle rocks, due to temperature and pressure variations during the simulations. We have constructed curves for solidus temperature (T_S) for lithospheric mantle, upper mantle and plume materials, based on data by Takahashi (1986), Takahashi et al. (1993) and Ueki and Iwamori (2013, 2014) and representative for fertile anhydrous peridotite (Fig. 2). A solidus temperature variation of +25 °C has been introduced for the melting curve of lithospheric mantle, in order to assess the higher melting temperature of depleted mantle material, in agreement with findings by Wasylenki et al. (2003). Likewise, a solidus temperature variation of −25 °C is considered for the mantle plume, assuming a lower T_S for more primitive material. Differently from T_S, in our model the liquidus temperature (T_L) curve is not subjected to variations depending on different materials. The liquidus temperature at pressure $P_0 = 0.1$ MPa is $T_l = 1860$ °C, relative to a Fo92 olivine composition in anhydrous conditions, while we assume that the Clapeyron slope for the Fo92 curve does not show significant variations from the Fo100 curve (Deer et al., 2013, and ref. therein). Based on the constructed curves, pressure-dependent solidus and liquidus temperatures are calculated at every time step to estimate the melt fraction φ occurring in mantle materials at different conditions of temperature and pressure.

The equations adopted in the model are polynomial and are the following (Fig. 2):

$$T_S = 0.03767P^4 - 1.02785P^3 + 2.53259P^2 + 124.9675P + 1125 \tag{17}$$

$$T_L = 48.5P + 1860 \tag{18}$$

where P is the pressure (expressed in GPa).

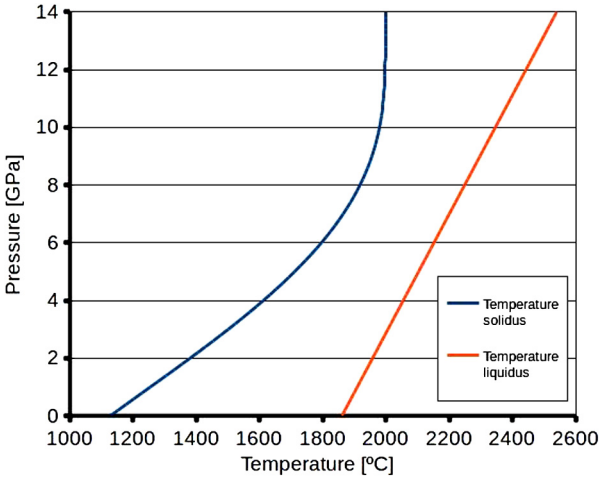

Fig. 2. Solidus and liquidus curves adopted in the model.

When the temperature of mantle rocks is in the range between solidus and liquidus temperature, the rocks are subjected to partial melting. The melt fraction produced is computed based on a linear interpolation between solidus and liquidus temperature:

$$T < T^S_{P,T} \rightarrow \varphi_{P,T} = 0 \tag{19}$$

$$T^S_{P,T} < T < T^L_{P,T} \rightarrow \varphi_{P,T} = \frac{T - T^S_{P,T}}{T^L_{P,T} - T^S_{P,T}} \tag{20}$$

$$T > T^L_{P,T} \rightarrow \varphi_{P,T} = 1 \tag{21}$$

where $\varphi_{P,T}$, $T^S_{P,T}$ and $T^L_{P,T}$ are pressure- and temperature-dependent melt fraction, solidus and liquidus temperatures, and T are temperature values registered in the mantle domain during each time step.

Melt production occurs at marker level, with a volume depending on the volume of the cell that contains them and the number of markers present in the cell at a given time step. The melt produced is collected and redistributed by markers at the level of melt neutral buoyancy (i.e. where the density of melts is equal to the host rock density), where the receiving markers store melt up to their total filling. When a receiving marker is full, the remaining melt is stored in the underlying marker, following a model of underplating by downward accretion (e.g. Annen, 2011). The melt movement occurs on a much shorter timescale than the velocity of rock deformation (e.g. Hawkesworth et al., 1997), due to its composition and its relative low viscosity (e.g. Dingwell, 1995). Consequently, magma transfer is assumed to be instantaneous.

At the emplacement level, the effect of melts affects both the plastic and the viscous behavior. In our model the effect of fluids on plastic strength follows the results by Rosenberg and Handy (2005), taking into account that a rock where melt presence exceeds $\varphi = 0.07$ is subjected to a decrease in strength. This effect is introduced by predicting a drop in the plastic yield strength, equal to one order of magnitude. Furthermore, the loss of cohesion caused by melt percolation in the intruded bodies has been incorporated, by introducing a viscosity drop down to $\mu = 10^{18}$ in the rock intervals where the quantity of melt exceeds the threshold RCMP = 35% vol. (Rheological Critical Melt Percentage, Arzi, 1978) and a temperature $T_T = 1100$ °C. In addition, the heat released during melt solidification also exerts a profound effect on the viscous strength of intruded rocks. We insert the term H_m in equation (7), quantifying the heat transported and released by moving melts:

$$H_m = \frac{\rho_m C_p (T_m - T_{hr})\varphi}{\Delta t} \tag{22}$$

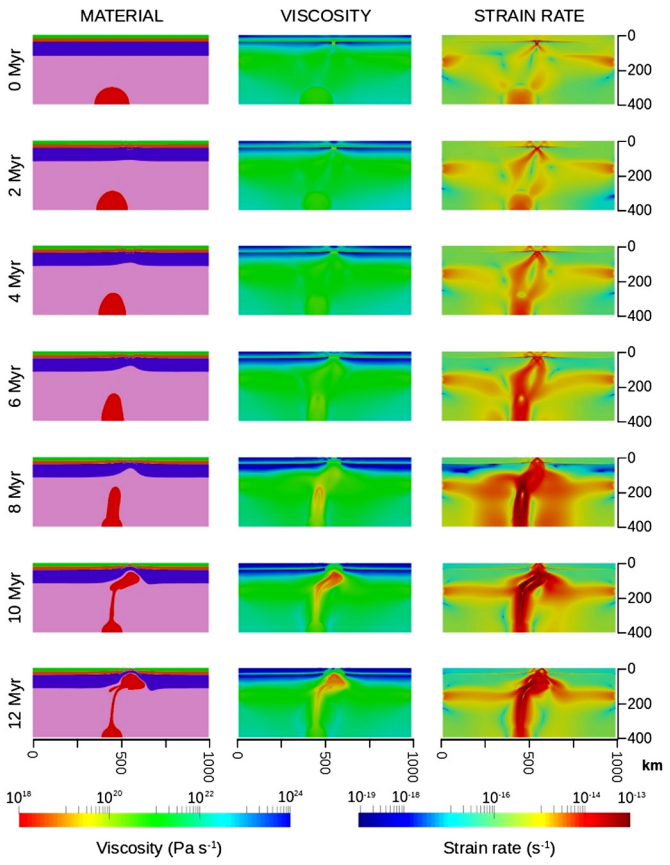

Fig. 3. Model results from the simulation set where 1) temperature at the base of the lithosphere is 1300 °C and temperature at the model base is 1475 °C, 2) melt is not included in the model and 3) Δ is 125 km. Dimensional values are expressed in km. Left column: material deformation (green: upper crust; orange: lower crust; violet: lithospheric mantle; pink: upper mantle; red: plume). Central column: viscosity values. Right column: strain rate values. Color scale in the central and right column is expressed as $\log_{10}$ of the obtained values. (For interpretation of the references to color in this figure legend, the reader is referred to the web version of this article.)

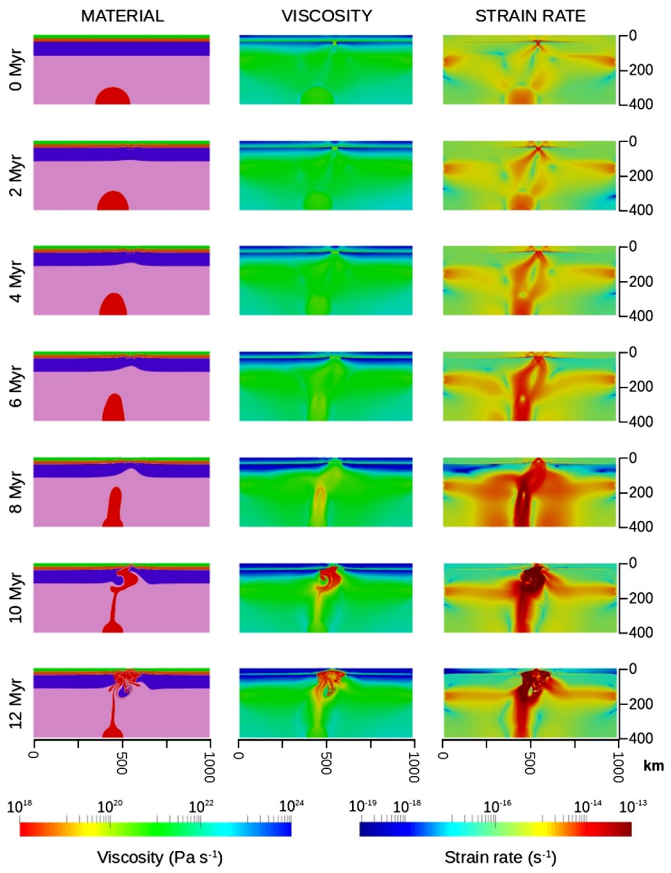

Fig. 4. Model results from the simulation set where 1) temperature at the base of the lithosphere is 1300 °C and temperature at the model base is 1475 °C, 2) melt is included in the model and 3) Δ is 125. Dimensional values are expressed in km. Left column: material deformation (green: upper crust; orange: lower crust; violet: lithospheric mantle; pink: upper mantle; red: plume). Central column: viscosity values. Right column: strain rate values. Color scale in the central and right column is expressed as $\log_{10}$ of the obtained values. (For interpretation of the references to color in this figure legend, the reader is referred to the web version of this article.)

where ρ_m, C_p, T_m and φ are respectively the density, heat capacity, emplacement temperature and melt fraction of the intruded melt, T_{hr} is the temperature of the host rocks at the moment of intrusion and Δt is the duration of the time step at the moment of H_m calculation (see Table 1 for a resume of the adopted values).

3. Results

The tested parameters are useful to highlight different features that characterize the lithosphere–plume interaction. This applies in particular to 1) relative plume–lithospheric discontinuity distance, and 2) different mantle temperature field. These parameters exert a key role in the final configuration and activity of rifting, including the location of melt underplating. Our model results are presented for models with and without melt generation, as sections for selected time steps (Figs. 3–7, 9), and topography profiles (Fig. 8). The time interval shown for each simulation set depends on the time needed for rifting to develop. According to the adopted configuration, it varies from 12 Myr to 24 Myr.

In all simulations two phases of rifting development can be distinguished. The first phase is characterized by uprising of plume material throughout the upper mantle, and the beginning of continental extension where the lithospheric weak zone is located. In this phase, although the lithospheric thinning and extension assumes "passive" rifting characteristics, the horizontal distance Δ between plume and lithospheric weakness affects a) the velocity of the plume material uprising, and b) the amount of lithospheric thinning in the rifting area.

For a Δ value of 125 km (Figs. 3, 4), the proximity of hot and weak mantle material to the rift axis determines a strain concentration along an interval connecting the rift and the plume tail. Consequently, after 7 Myr the rising mantle material experiences an acceleration, leading to a plume impact against the lithosphere between 8 Myr and 9 Myr. This is the case study when we have registered the fastest velocities of plume uprising and interaction with the lithosphere. At the same time, high temperatures and strain rates experienced in the mantle wedge beneath the rifting area determine a stronger decrease in viscosity than in other simulations. This results in a very effective thinning of the lithospheric mantle, by a factor of more than 2 at the location of the rift. To give a comparison, in the simulation sets where the value of Δ is increased, the impact age of plume material against the lithosphere is delayed and occurs after 11 Myr (Fig. 5). This is due to lower temperatures and strain rates recorded in the mantle interval between the plume and the lithosphere discontinuity. In addition, with increasing Δ values, the amount of lithospheric thinning is drastically reduced, becoming modest when $\Delta = 500$ km (Figs. 6, 7).

The second phase of rift development is subsequent to the impact of plume material below the lithosphere, sometime between 8 Myr and 11 Myr from the onset of the simulations, depending on the adopted Δ value. In this phase, different Δ values deter-

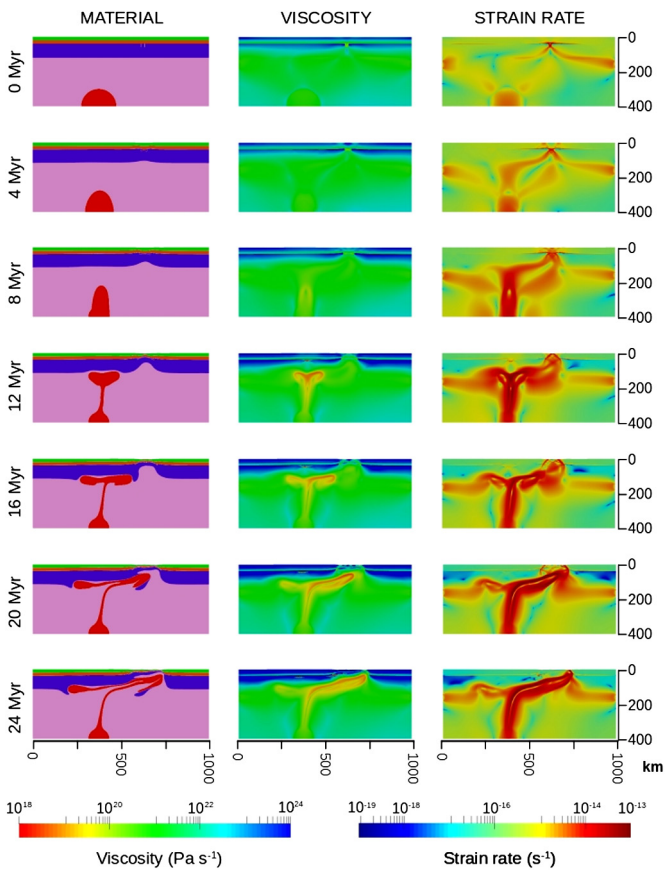

Fig. 5. Model plots resulting from the simulation set where 1) temperature at the base of the lithosphere is 1300 °C and temperature at the model base is 1475 °C, 2) melt is included in the model and 3) Δ is 250 km. The same model configuration shows negligible variations when melting is incorporated. Dimensional values are expressed in km. Left column: material deformation (green: upper crust; orange: lower crust; violet: lithospheric mantle; pink: upper mantle; red: plume). Central column: viscosity values. Right column: strain rate values. Color scale in the central and right column is expressed as $\log_{10}$ of the obtained values. (For interpretation of the references to color in this figure legend, the reader is referred to the web version of this article.)

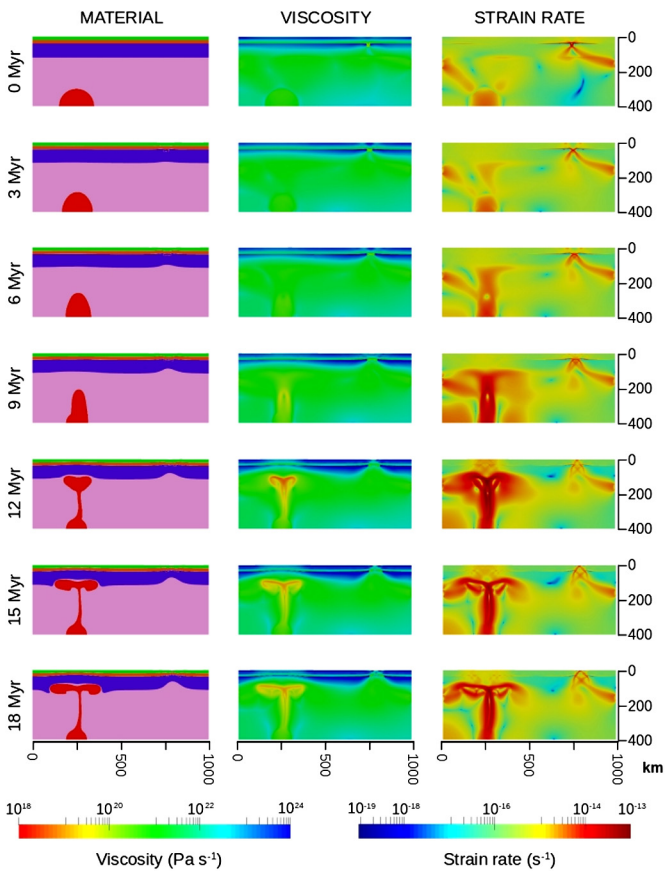

Fig. 6. Model plots resulting from the simulation set where 1) temperature at the base of the lithosphere is 1300 °C and temperature at the model base is 1475 °C, 2) melt is not included in the model and 3) Δ is 500 km. Dimensional values are expressed in km. Left column: material deformation (green: upper crust; orange: lower crust; violet: lithospheric mantle; pink: upper mantle; red: plume). Central column: viscosity values. Right column: strain rate values. Color scale in the central and right column is expressed as $\log_{10}$ of the obtained values. (For interpretation of the references to color in this figure legend, the reader is referred to the web version of this article.)

mine more profound variations of the rift style than in the first phase. When $\Delta = 125$ km (Fig. 3), we observe, in a time span of about 1 Myr, a channeling of plume material in the area previously occupied by the upper mantle wedge, with subsequent very high temperatures and strain rates. In this model, the mantle wedge beneath the rifting area experiences a temperature peak in proximity of the rift side opposite to the one directly impinged by the plume. On the other hand, in the same mantle wedge the highest values of strain rate are localized around the area of plume impingement. This leads to viscosity values in the mantle that are almost symmetric with respect to the rift axis, and to a roughly symmetric thinning of the lithosphere, only slightly more pronounced in the rift axis directly above the plume impact point.

When $\Delta = 250$ km (Fig. 5), the plume exerts a pronounced erosion on the lithospheric mantle on both developed margins, which show a marked asymmetry in plate thickness. Between 19 Myr and 20 Myr after the onset of simulation, part of plume material is channeled through the lithosphere into the asthenospheric wedge beneath the rifting area, with associated delamination of the lithospheric mantle. As a consequence, the plate half-space previously unaffected by the plume presence is now subjected to erosion, with subsequent migration of the rifting area away from the plume. For $\Delta = 500$ km, the lithosphere discontinuity and the plume do not interact (Fig. 6): the former gives rise to a moderate lithospheric thinning and incipient rift system, while the latter proceeds with lithospheric mantle erosion, accompanied by a slight topographic swelling and crustal thinning. Differently from the previous simulation sets, the plate segment between the plume and the lithospheric discontinuity is relatively undeformed (with recorded strain rate values one magnitude order lower than in the rifting areas), and not subjected to any relevant strain rate for the whole simulation history.

The results above can significantly vary when the melt effect is introduced in the simulations, based on the value of the parameter Δ. In all simulations (Figs. 4, 5, 7), the plume is the material subjected to melting, occurring at a depth not greater than 150 km. The start of melt generation slightly post-dates the beginning of lithospheric thermal erosion: this indicates that a previous (although moderate) lithospheric thinning is needed for the beginning of melting in the plume. When the rifting area and the plume impact point on the lithosphere are very close ($\Delta = 125$ km) (Fig. 4), the melt impinged at the base of the lithosphere causes a drop in viscosity values and a dramatic increase of strain rate values on the site where the plume impacts. This determines a more pronounced asymmetric erosion of the mantle lithosphere with respect to the same case study in absence of melt generation, and is accompanied by a marked lithospheric delamination. The emplacement of plume material into the lithosphere occurs through many distinct batches, each of them distinguishable also by different degrees of partial melting (which could reflect into different phases of magmatic activity). However, the asymmetry of the generated

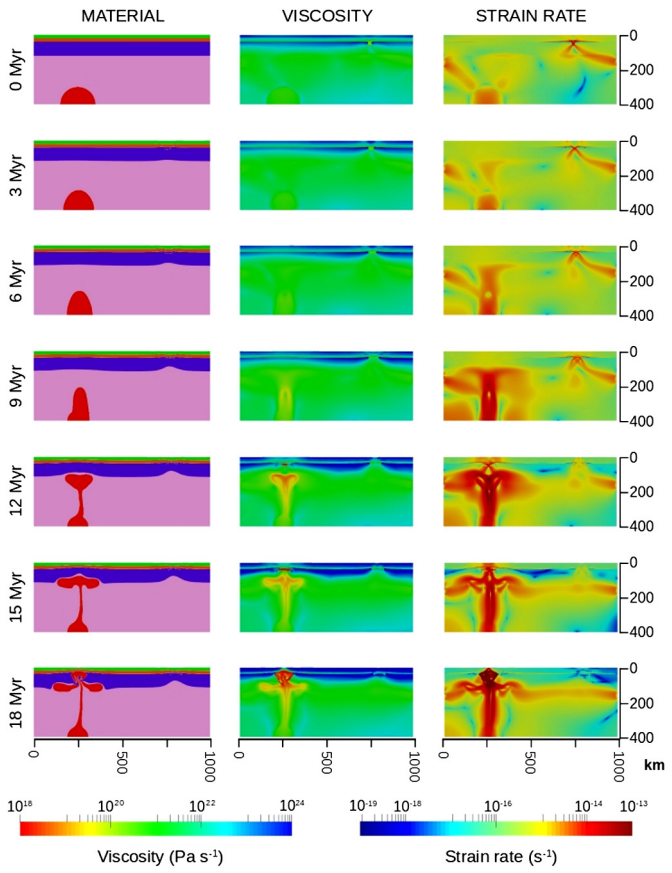

Fig. 7. Model plots resulting from the simulation set where 1) temperature at the base of the lithosphere is 1300 °C and temperature at the model base is 1475 °C, 2) melt is included in the model and 3) Δ is 500 km. Dimensional values are expressed in km. Left column: material deformation (green: upper crust; orange: lower crust; violet: lithospheric mantle; pink: upper mantle; red: plume). Central column: viscosity values. Right column: strain rate values. Color scale in the central and right column is expressed as $\log_{10}$ of the obtained values. (For interpretation of the references to color in this figure legend, the reader is referred to the web version of this article.)

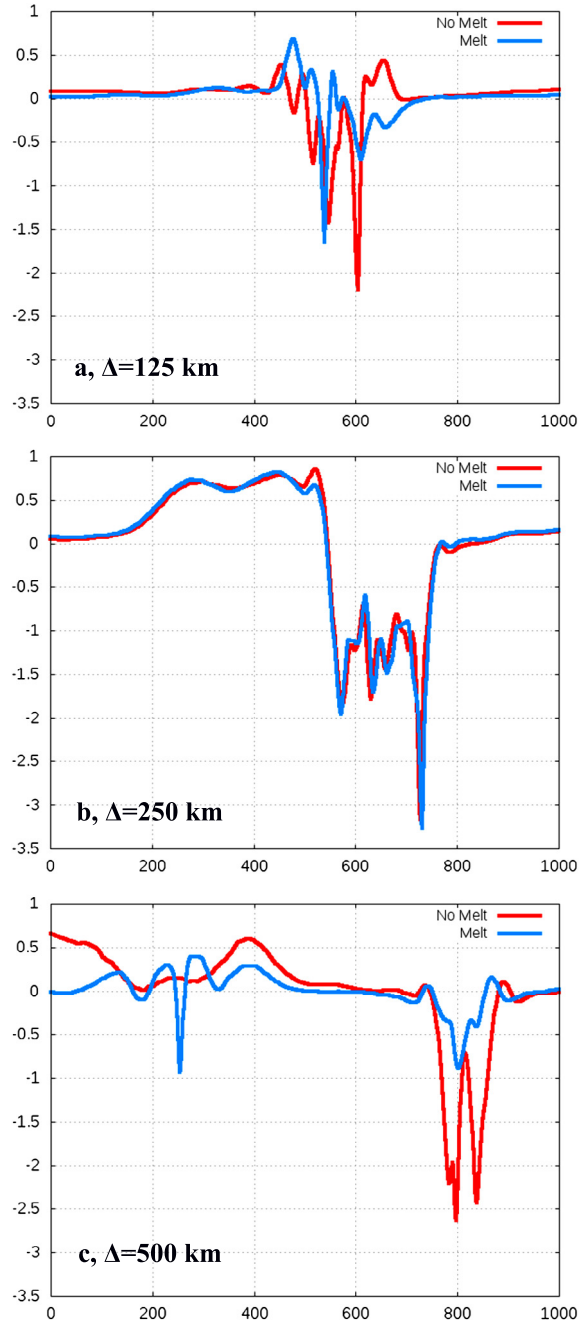

Fig. 8. Final topographic profiles obtained for different simulation sets, based on plume–lithospheric weak zone distance (Δ) of a) 125 km, b) 250 km and c) 500 km. Dimensional scales are expressed in km. Red lines: case studies where melt is not included in the simulation; blue lines: case studies where melt is included in the simulation. (For interpretation of the references to color in this figure legend, the reader is referred to the web version of this article.)

rifting is not expressed by the topography, except for a less accentuated depression in the rifting structure, toward the area where the plume impinges the lithosphere (Fig. 8).

If the distance Δ is increased to a value of 250 km (Fig. 5), the melt underplating starts at the plume impingement point, and subsequently propagates towards the area of lithospheric extension. However, in this simulation set the presence of melt does not cause a drop in viscosity, despite its abundance, except for very small intervals. This occurs because melts generated by plume material channeled into the rifting area are widely distributed along the lithosphere. Consequently, the local volume of melt is smaller than in the previous case, and their temperature is above the solidus for a very limited time span. Thus, the viscosity does not drop sufficiently long to cause the initiation of other potential rifts. This response is also reflected by the topography, which is similar for the simulation sets with and without melt generation (Fig. 8).

For $\Delta = 500$ km, the strain concentrates in the first 11 Myr in proximity of the lithospheric weakness, leading to necking of the lithosphere (Fig. 7). At this time, we predict the first presence of melts at the Moho, with associated drop in viscosity. This leads to a fast strain transfer from the previous location of lithospheric thinning and extension to a new location, above the plume impingement point. The very high temperatures reached and the accumulation of melt in this location greatly contribute to the concentration of strain in this new rifting area. The process of lithosphere erosion becomes particularly efficient after 15 Myr, when the lithosphere has been almost completely penetrated by plume material. The activation of this rifting area implies the abandonment of the previous rifting location, that becomes progressively inactive. The importance of the melt contribution can also be noticed from the topographic trend of the model free surface (Fig. 8): in the melt simulation set, the model predicts two rift structures of similar depth, whereas if melts are not included in the simulations a very deep rift is associated with a moderate topographic swell.

When a colder mantle geotherm and plume temperature are adopted, the model predicts a marked increase in viscosity for both upper mantle and plume, with an associated decrease in

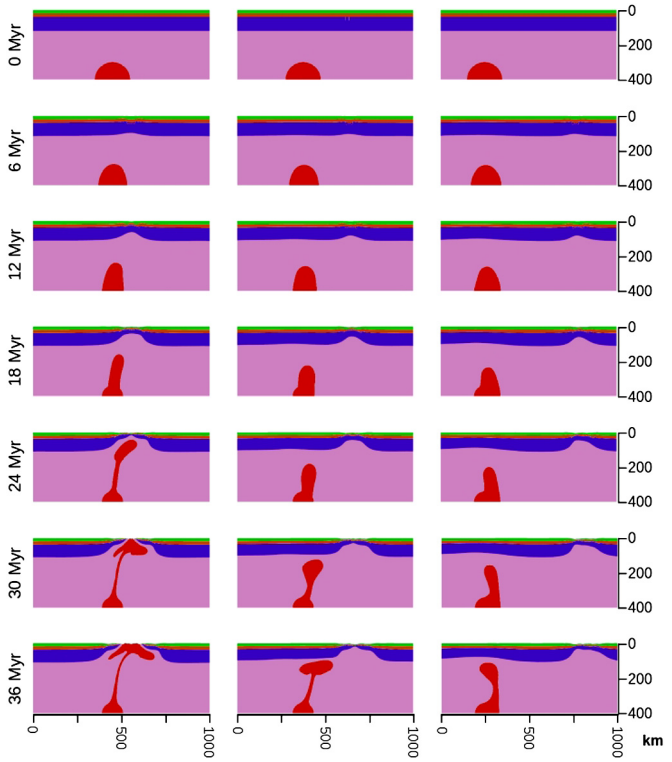

Fig. 9. Cross-section plots resulting from the simulation set where 1) temperature at the base of the lithosphere is 1200 °C and temperature at the model base is 1400 °C, 2) melt is included in the model and 3) Δ is 125 km (left column), 250 km (central column) and 500 km (right column). Dimensional values are expressed in km. Images display material deformation. Green: upper crust; orange: lower crust; violet: lithospheric mantle; pink: upper mantle; red: plume. (For interpretation of the references to color in this figure legend, the reader is referred to the web version of this article.)

plume uprising velocity. This contributes to a further cooling of the plume material before reaching the base of the lithosphere. Therefore, the lithospheric erosion is not as effective as in the previous simulation sets, and occurs about 10 Myr after the onset of plate thinning (Fig. 9). In addition, when the plume impacts the lithosphere, it is effectively channeled into the center of an already well delineated rift system, even though the decompression-related partial melting does not occur only along the rift axis, but is more concentrated along the lithosphere directly above the plume. Our model predicts an asymmetric melt distribution for Δ less than 250 km, despite that low temperature and increased viscosity do not favor any pronounced asymmetry of passive continental margins. If Δ is increased to a value of 500 km, the rifting is completely controlled by the presence of the lithospheric weakness, with the presence of a plume causing plate thinning at the impact point ($\beta_{\text{lithosphere}} < 1.4$) and negligible topographic swelling.

4. Discussion

In our model the effectiveness of thermo-mechanical erosion due to the plume impact over the lithosphere mostly depends on two parameters: 1) the relative lateral distance between plume and lithospheric thinning area, and 2) the upper mantle and plume temperature (hence, viscosity). In addition, a novel aspect of this study with respect to previous papers is a quantification of the strength reduction on the host rocks, caused by melt intrusion. If the effect of melts is not incorporated in the simulations, the lithospheric strength reduction related to plume erosion is generally modest, in agreement with findings by Brune et al. (2013). This leads to a controlling role of the pre-existing lithospheric structure in determining the location of thinning and extension: we have observed that when models do not include the possibility of melting for mantle materials, the presence of zones of strain localization is pivotal for the development of rifted basins, in agreement with Franke (2012) and Koptev et al. (2015). At short distances between lithospheric heterogeneities and plume, the lithospheric structure affects the pattern of the rising plume in the upper mantle, since it determines the location where the asthenospheric wedge that underlies the lithospheric rift occurs. In such conditions, the plume head flattens at the lithosphere–mantle boundary, in agreement with previous findings (Burov et al., 2007; Guillou-Frottier et al., 2012; Burov and Gerya, 2014; Koptev et al., 2015), resulting in delamination in the lithospheric mantle (e.g. Burov and Gerya, 2014) that becomes progressively asymmetric in the process. Lithosphere erosion is preferentially concentrated at the top of the plume impact point, and is accompanied by down-thrusting at both sides of the flattening plume head.

In cases where the lithospheric weakness plays a key role in the location of the rifting area, the contribution given by the buoyancy forces associated with the plume presence may strongly influence the characteristics of rifts during their evolution. According to Huismans et al. (2001), the forces associated with the asthenosphere impingement beneath the lithosphere may become equal to far field forces, or even predominant, in post-rift phases. Our model shows that when the distance between plume and lithospheric extensional area is equal or less than 250 km, the plume presence causes fast lithospheric consumption, that favors the growth of the asthenospheric wedges beneath the rifting area. Furthermore, the asymmetric thickness variations of the lithosphere–asthenosphere boundary (LAB) caused by the plume (including the lithospheric down-thrusting at the sides of the plume head) may lead to a steady-state migration of the rifting and the creation of asymmetric margins, with one margin hyper hyper-extended (as defined e.g. in Tugend et al., 2015). Asymmetric margins are not uncommon (e.g. Gaina et al., 2007) and have been already reproduced in numerical models (e.g. Brune et al., 2014), but we suggest that plumes may also play a role in their development and evolution. In addition, plume material may be channeled away from the lithosphere impingement point, across the lithosphere and toward the rifting area, and erode the lithosphere on the opposite rifting margin. The resulting erosive effect, coupled with the plate-related far field stresses, promotes the asymmetry of the two margins and the migration of the rifting area far from the plume. This integrates the results obtained by Brune et al. (2016), where a marked asymmetry developed in passive continental margins promotes rifting migration at later stages.

The effects of melting on rift evolution show a marked dependence on both the distance between the plume and lithospheric weak zones and the upper mantle thermal state, but this relationship is not simple to predict. When the plume is located in proximity of the lithospheric heterogeneity, plume material is directly channeled in the asthenospheric rifting wedge, with subsequent high temperature and upwelling velocity. Consequently, temperatures predicted in the plume are high enough to allow extensive partial melting of mantle materials. In this context, the large amount of melt intruded at the crust–mantle boundary determines a marked viscosity drop and leads to a very effective lithospheric mantle delamination. This is mostly concentrated on the rifting margin where the plume directly impacts against the lithosphere. The consequences of this asymmetric distribution of lithospheric erosion are two-fold: 1) this may lead to an asymmetric distribution of volcanism, and 2) the very effective replacement of the lithosphere by hotter and less dense plume material may lead to

a topographic swelling at the rifting margin where the plume is located.

Asymmetric distribution of volcanism along magmatic passive margins was observed in previous studies (e.g. Holbrook et al., 2001). However, melt underplating strongly favors the possibility of magmatic activity concentrated along one of the two margins: when melt is not included, the plume material is directly channeled in the asthenospheric wedge with minimum asymmetric erosion of the plate margins, due to the high viscosity of the lithosphere. Differently, when melt underplating occurs, the viscosity drop due to the loss of cohesion in the lithosphere determines a strong concentration of strain in the passive continental margin where the plume is present. This, however, does not promote rifting migration when lithosphere weak zones and plume are very close, because plume material is still effectively channeled in the asthenospheric wedge, which is connected to the lithospheric heterogeneity. Consequently, most erosional effects by the plume material are still confined to the initial extensional area. In addition, when melting is included in the model, temperatures reached in the crust are favorable for an extended anatexis, with subsequent silicic volcanism. Although poorly preserved in the stratigraphic record, silicic melts and volcanic products may constitute a large part of the eruptive stratigraphy (e.g. Bryan et al., 2002), and, at crustal levels, the presence of acidic melts contributes to rock strength decrease (Arzi, 1978; Rosenberg and Handy, 2005; Lavecchia et al., 2016a, 2016b).

When the distance between lithospheric heterogeneities and plume promotes a marked asymmetry in the conjugate margin system, our model indicates a spreading mechanism affecting the melt underplating and the subsequent eruptive and effusive activity. This results in a younging direction of magmatic bodies constituting the Seaward Dipping Reflectors (SDR, e.g. Abdelmalak et al., 2016) towards the rift center, and accompanying/post-dating the development of passive margins. On the other hand, when melt underplating occurs along a passive margin where the lithosphere is strongly thinned (Fig. 5), temperatures reached at the Moho along the margins are relatively low. As a result, melt intruded at the base of the lithosphere may solidify in a short time span, thus not playing a determinant role for the geodynamic evolution of the margin.

When plume material does not directly interact with areas of lithospheric extension (Fig. 7), our model shows a major role of melt underplating for the evolution of passive margins. The presence of melts may determine a strong decrease in lithospheric strength along the underplated intervals. In such conditions, the initial rift developed at the location favored by lithosphere structural control may be abandoned and the plume assumes a dominant role. The association between rifting areas and plume, with subsequent rift jumps and abandoned rifting branches, is observed in many locations, including Iceland (e.g. Garcia et al., 2003), the South Atlantic (Brozena and White, 1990) and the Galapagos spreading center (Wilson and Hey, 1995). According to our findings, the process of rift jump is not linear, but follows a two-step process: during a first stage the plume erodes the lithosphere and reaches a depth favorable for the beginning of decompression melting; afterwards, the melt underplated at the crust–lithosphere boundary leads to a strength drop sufficient for plate break-up to occur. This leads to an extended magmatism where the plume impacts the lithosphere, and the strength decrease in the lithosphere may favor a symmetric evolution of the passive continental margins (see Brune et al., 2016). However, 3D modelling will be important to determine if a plume-related rift is not constrained only in proximity of the plume but may lead also to a plate-scale rifting system (e.g. Burov and Gerya, 2014).

5. Conclusions

The interaction between a structurally complex lithosphere and plumes is not simple to predict. A further source of complexity is added when melt presence is taken into account during the study of passive margins characteristics. Our study shows that the configuration of a rifting area may be influenced by the topography of the lithosphere–asthenosphere boundary, thermal state of the mantle and plume presence at different stages of its evolution, and that presence of melts may have a great impact on the resulting characteristics of passive margins.

The lateral distance between main areas of lithospheric heterogeneity and plumes is a parameter of primary importance for rifting evolution. Lithosphere weak zones determine the location for initial plate breakup, that may persist in the same area for an extended period. Subsequently, our model predicts a close interaction between the rift area generated by passive stresses and the presence of plumes. When the plume is close enough to be channeled into the rift, the effects of active and passive stress fields sum up, resulting in an acceleration of lithosphere erosion. In the absence of mantle melting, the erosion is characterized by features that depend on the initial distance between plumes and lithospheric heterogeneities: a small distance favors the development of symmetric passive margins, whereas a greater distance is more favorable for asymmetric margins. On the other hand, when a plume is not channeled into areas of lithospheric thinning, and in absence of melting, its presence does not cause main effects on lithospheric rifting evolution.

Melts may substantially impact the evolution of passive continental margins, when the melt presence exceeds a threshold sufficient to cause a strength drop in the lithosphere, but their role also depends on the relative position of plumes with respect to the rifting area. Melt underplating may favor the evolution of asymmetric passive margins, independently from the pre-existing structure of the lithosphere, and appears a key factor in the erosion of the lithosphere caused by plumes: this effect may be so intense that well delineated rifts may be abandoned and new areas of lithospheric breakup may develop over intensely underplated lithospheric intervals, with consequent jumps in rift formation.

Acknowledgements

This study was funded by Simula School of research and Innovation, P.O. Box 134, 1325 Lysaker, Norway, and the Netherlands Research Center for Integrated Solid Earth Science. The data for this paper are available by contacting the corresponding author.

References

Abdelmalak, M.M., Planke, S., Faleide, J.I., Jerram, D.A., Zastrozhnov, D., Eide, S., Myklebust, R., 2016. The development of volcanic sequences at rifted margins: new insights from the structure and morphology of the Vøring Escarpment, mid-Norwegian Margin. J. Geophys. Res. (ISSN 2169-9313). http://dx.doi.org/10.1002/2015JB012788.

Annen, C., 2011. Implications of incremental emplacement of magma bodies for magma differentiation, thermal aureole dimensions and plutonism–volcanism relationships. Tectonophysics 500, 3–10.

Arzi, A., 1978. Critical phenomena in the rheology of partially melted rocks. Tectonophysics 44, 173–184.

Bosworth, W., Huchon, P., McClay, K., 2005. The Red Sea and Gulf of Aden Basins. J. Afr. Earth Sci. 43, 334–378.

Bott, M.H.P., Kusznir, N.J., 1979. Stress distribution associated with compensated plateau uplift structures with application to the continental splitting mechanism. Geophys. J. R. Astron. Soc. 56, 451–459.

Brozena, J.M., White, R.S., 1990. Ridge jumps and propagations in the South Atlantic Ocean. Nature 348, 149–152.

Brune, S., Popov, A.A., Sobolev, S.V., 2013. Quantifying the thermo-mechanical impact of plume arrival on continental break-up. Tectonophysics 604, 51–59. http://dx.doi.org/10.1016/j.tecto.2013.02.009.

Brune, S., Heine, C., Pèrez-Gussinyè, M., Sobolev, S., 2014. Rift migration explains continental margin asymmetry and crustal hyperextension. Nat. Commun. 5, 4014. http://dx.doi.org/10.1038/ncomms5014.

Brune, S., Heine, C., Clift, P.D., Pèrez-Gussinyè, M., 2016. Rifted margin architecture and crustal rheology: reviewing Iberia–Newfoundland, central South Atlantic, and South China Sea. Mar. Pet. Geol. 79, 257–281. http://dx.doi.org/10.1016/j.marpetgeo.2016.10.018.

Bryan, S.E., Riley, T.R., Jerram, D.A., Stephens, C.J., Leat, P.T., 2002. Silicic volcanism: an undervalued component of large igneous provinces and volcanic rifted margins. In: Geol. Soc. Am. Spec. Pap., vol. 362, pp. 99–120.

Buck, W.R., 2004. Consequences of asthenospheric variability on continental rifting. In: Karner, G.D., Taylor, B., Driscoll, N.W., Kohlstedt, D.L. (Eds.), Rheology and Deformation of the Lithosphere at Continental Margins. Columbia Univ. Pr., pp. 1–31.

Burov, E., Gerya, T., 2014. Asymmetric three-dimensional topography over mantle plumes. Nature 513, 85–89. http://dx.doi.org/10.1038/nature13703.

Burov, E., Guillot-Frottier, L., d'Acremont, E., Le Pourhiet, L., Cloetingh, S., 2007. Plume head–lithosphere interactions near intra-continental plate boundaries. Tectonophysics 434, 15–38. http://dx.doi.org/10.1016/j.tecto.2007.01.002.

Chorowicz, J., Collet, B., Bonavia, F., Mohr, P., Parrot, J.F., Korme, T., 1998. The Tana basin, Ethiopia: intra-plateau uplift, rifting and subsidence. Tectonophysics 295, 351–367.

Cloetingh, S.A.P.L., Wortel, R., 1986. Stress in the Indo–Australian plate. Tectonophysics 132, 49–67.

Deer, W.A., Howie, R.A., Zussman, J., 2013. An Introduction to the Rock-Forming Minerals. Mineral. Soc., London, UK. 498 pp.

Dingwell, D., 1995. Viscosity and anelasticity of melts. In: Ahrens, T.J. (Ed.), Mineral Physics and Crystallography. A Handbook of Physical Constants. In: AGU Reference Shelf 2. Am. Geophys. Union, Washington, DC, pp. 209–217.

Einardsson, P., 2008. Plate boundaries, rifts and transforms in Iceland. Jökull 58, 35–58.

Fischer, R., Gerya, T., 2016. Early Earth plume-lid tectonics: a high resolution 3D numerical modelling approach. J. Geodyn. 100, 198–214. http://dx.doi.org/10.1016/j.jog.2016.03.004.

Franke, D., 2012. Rifting, lithosphere breakup and volcanism: comparison of magma-poor and volcanic rifted margins. Mar. Pet. Geol. 43, 63–87. http://dx.doi.org/10.1016/j.marpetgeo.2012.11.003.

Gaina, C., Muller, R.D., Brown, B., Ishihara, T., Ivanov, S., 2007. Breakup and early seafloor spreading between India and Antarctica. Geophys. J. Int. 170, 151–169.

Garcia, S., Arnaud, N.O., Angelier, J., Bergerat, F., Homberg, C., 2003. Rift jump process in Northern Iceland since 10 Ma from $^{40}Ar/^{39}Ar$ geochronology. Earth Planet. Sci. Lett. 214, 529–544.

Gerya, T., 2010. Introduction to Numerical Geodynamic Modelling. Cambridge Univ. Press, UK. 345 pp.

Gleason, G.C., Tullis, J., 1995. A flow law for dislocation creep of quartz aggregates determined with the molten salt cell. Tectonophysics 247, 1–23.

Guillou-Frottier, L., Burov, E., Cloetingh, S., Le Goff, I., Deschamps, Y., Huet, B., Bouchot, V., 2012. Plume-induced dynamic instabilities near cratonic blocks: implications for P–T–t paths and metallogeny. Glob. Planet. Change 90–91, 37–50.

Hawkesworth, C.J., Turner, S.P., McDermott, F., Peate, D.W., van Calsteren, P., 1997. U–Th isotopes in arc magmas: implications for element transfer from the subducted crust. Science 276, 551–555.

Hill, R.I., 1991. Starting plumes and continental break-up. Earth Planet. Sci. Lett. 104, 398–416.

Holbrook, W.S., Larsen, H.C., Korenaga, J., Dahl-Jensen, T., Reid, I.D., Kelemen, P.B., Hopper, J.R., Kent, G.M., Lizarralde, D., Bernstein, S., Detrick, R.S., 2001. Mantle thermal structure and active upwelling during continental breakup in the North Atlantic. Earth Planet. Sci. Lett. 190, 251–266.

Huismans, R.S., Podladchikov, Y.Y., Cloetingh, S., 2001. Transition from passive to active rifting: relative importance of asthenospheric doming and passive extension of the lithosphere. J. Geophys. Res. 106 (B6), 11271–11291.

Huismans, R.S., Beaumont, C., 2011. Depth-dependent extension, two-stage breakup and cratonic underplating at rifted margins. Nature 473, 74–79. http://dx.doi.org/10.1038/nature09988.

Kachanov, L., 2004. Fundamentals of the Theory of Plasticity. Dover Publ. Inc., N.Y. 512 pp.

Karato, S.I., Wu, P., 1993. Rheology of the upper mantle: a synthesis. Science 260, 771–778.

Koptev, A., Calais, E., Burov, E., Leroy, S., Gerya, T., 2015. Dual continental rift systems generated by plume–lithosphere interactions. Nat. Geosci. 8, 388–392. http://dx.doi.org/10.1038/NGEO2401.

Lavecchia, A., Clark, S., Beekman, F., Cloetingh, S., Burov, E., 2016a. Thermal perturbation, mineral assemblages and rheology variations induced by dyke emplacement in the crust. Tectonics 35. http://dx.doi.org/10.1002/2016TC004125.

Lavecchia, A., Clark, S., Beekman, F., Cloetingh, S., 2016b. Thermo-rheological aspects of crustal evolution during continental breakup and melt intrusion: the Main Ethiopian Rift, East Africa. Tectonophysics 686, 51–62. http://dx.doi.org/10.1016/j.tecto.2016.07.018.

McClusky, S., Reilinger, R., Ogubazghi, G., Amleson, A., Healeb, B., Vernant, P., Sholan, J., Fisseha, S., Asfaw, L., Bendick, R., Kogan, L., 2010. Kinematics of the southern Red Sea–Afar Triple Junction and implications for plate dynamics. Geophys. Res. Lett. 37, L05301. http://dx.doi.org/10.1029/2009GL041127.

Menzies, M., Klemperer, S., Ebinger, C., Baker, J., 2002. Characteristics of volcanic rifted margins. In: Menzies, M., Klemperer, S., Ebinger, C., Baker, J. (Eds.), Volcanic Rifted Margins. In: Geol. Soc. Am. Spec. Paper, vol. 362, pp. 1–14.

Mittelstaedt, E., Ito, G., Behn, M.D., 2008. Mid-ocean ridge jumps associated with hotspot magmatism. Earth Planet. Sci. Lett. 266, 256–270. http://dx.doi.org/10.1016/j.epsl.2007.10.05.

Philpotts, A.R., Ague, J.J., 2009. Principles of Igneous and Metamorphic Petrology. Camb. Univ. Press, Cambridge, UK. 667 pp.

Rosenberg, C.L., Handy, M.R., 2005. Experimental deformation of partially melted granite revisited: implications for the continental crust. J. Metamorph. Geol. 23, 19–28.

Rybacki, E., Dresen, G., 2000. Dislocation and diffusion creep of synthetic anorthite aggregates. J. Geophys. Res. 105 (260), 17–36.

Schubert, G., Turcotte, D., Olson, P., 2001. Mantle Convection in the Earth and Planets. Cambridge University Press, UK. 940 pp.

Svartman Dias, A.E., Lavier, L.L., Hayman, N.W., 2015. Conjugate rifted margins width and asymmetry: the interplay between lithospheric strength and thermomechanical processes. J. Geophys. Res., Solid Earth 120, 8672–8700. http://dx.doi.org/10.1002/2015JB012074.

Takahashi, E., 1986. Melting of a Dry Peridotite KLB-1 up to 14 GPa: implications on the Origin of Peridotitic Upper Mantle. J. Geophys. Res. 91 (B9), 9367–9382.

Takahashi, E., Shimazaki, T., Tsuzaki, Y., Yoshida, H., 1993. Melting study of a peridotite KLB-1 to 6.5 GPa, and the origin of basaltic magmas. Philos. Trans. R. Soc. Lond. 342, 105–120.

Thieulot, C., 2011. FANTOM. Two- and three-dimensional numerical modelling of creeping flows for the solution of geological problems. Phys. Earth Planet. Inter. 188, 47–68. http://dx.doi.org/10.1016/j.pepi.2011.06.011.

Tugend, J., Manatschal, G., Kusznir, N.J., 2015. Spatial and temporal evolution of hyperextended rift systems: implication for the nature, kinematics, and timing of the Iberian–European plate boundary. Geology 43, 15–19. http://dx.doi.org/10.1130/G36072.1.

Ueki, K., Iwamori, H., 2013. Thermodynamic model for melting of peridotite. Geochem. Geophys. Geosyst. 14, 342–366. http://dx.doi.org/10.1029/2012GC004143.

Ueki, K., Iwamori, H., 2014. Thermodynamic calculations of the polybaric melting phase relations of spinel lherzolite. Geochem. Geophys. Geosyst. 15, 5015–5033. http://dx.doi.org/10.1002/2014GC005546.

Wasylenki, L.E., Baker, M.B., Kent, A.J.R., Stolper, E.M., 2003. Near-solidus melting of the shallow upper mantle: partial melting experiments on depleted peridotite. J. Petrol. 44 (7), 1163–1191.

White, R.S., McKenzie, D., 1989. Magmatism at rift zones: the generation of volcanic continental margins and flood basalts. J. Geophys. Res. 94, 7685–7729.

Wilson, D.S., Hey, R.N., 1995. History of rift propagation and magnetization intensity for the Cocos–Nazca spreading center. J. Geophys. Res. 100 (B6), 10,041–10,056. http://dx.doi.org/10.1029/95JB00762.

Wolfenden, E., Ebinger, C., Yirgu, G., Deino, A., Ayalew, D., 2004. Evolution of the northern Main Ethiopian rift: birth of a triple junction. Earth Planet. Sci. Lett. 224, 213–228. http://dx.doi.org/10.1016/j.epsl.2004.04.022.

Wright, T.J., Freysteinn, S., Pagli, C., Belachew, M., Hamling, I.J., Brandsdóttir, B., Keir, D., Pedersen, R., Ayele, A., Ebinger, C., Einarsson, P., Lewi, E., Calais, E., 2012. Geophysical constraints on the dynamics of spreading centres from rifting episodes on land. Nat. Geosci. 5, 242–250. http://dx.doi.org/10.1038/NGEO1428.

Ziegler, P.A., Cloetingh, S., 2004. Dynamic processes controlling evolution of rifted basins. Earth-Sci. Rev. 64, 1–50.